BNL-82133-2009-CP

Effects of Te inclusions on the performance of CdZnTe radiation detectors

A. E. Bolotnikov, N. M. Abdul-Jabber, O. S. Babalola, G. S. Camarda, Y. Cui, A. M. Hossain, **E. M. Jackson, H. C. Jackson, J. A. James**, K. T. Kohman, **A. L. Luryi, and R. B. James**

Presented at the 2008 IEEE Conference
Dresden, Germany
October 19-25, 2008

January 2009

Nonproliferation and National Security Department

Brookhaven National Laboratory
P.O. Box 5000
Upton, NY 11973-5000
www.bnl.gov

DISCLAIMER

Effects of Te inclusions on the performance of CdZnTe radiation detectors

A. E. Bolotnikov, *Member, IEEE*, N. M. Abdul-Jabber, O. S. Babalola, G. S. Camarda, Y. Cui, *Member, IEEE*, A. M. Hossain, E. M. Jackson, H. C. Jackson, J. A. James, K. T. Kohman, A. L. Luryi, and R. B. James, *Fellow, IEEE*

***Abstract*—Te inclusions existing at high concentrations in CdZnTe (CZT) material can degrade the performance of CZT detectors. These microscopic defects trap the free electrons generated by incident radiation, so entailing significant fluctuations in the total collected charge and thereby strongly affecting the energy resolution of thick (long-drift) detectors. Such effects were demonstrated in thin planar detectors, and, in many cases, they proved to be the dominant cause of the low performance of thick detectors, wherein the fluctuations in the charge losses accumulate along the charge's drift path. We continued studying this effect using different tools and techniques. We employed a dedicated beam-line recently established at BNL's National Synchrotron Light Source for characterizing semiconductor radiation detectors, along with an IR transmission microscope system, the combination of which allowed us to correlate the concentration of defects with the devices' performances. We present here our new results from testing over 50 CZT samples grown by different techniques. Our goals are to establish tolerable limits on the size and concentrations of these detrimental Te inclusions in CZT material, and to provide feedback to crystal growers to reduce their numbers in the material.**

***Index Terms*—CdZnTe, radiation detectors, Te inclusions**

Introduction

LARGE effective volume CdZnTe (CZT) detectors are in great demand in many areas of x- and gamma-ray imaging and spectroscopy [1]. However, there still are obstacles limiting the wide use of this promising technology [2-5]. Recently, evidence has shown that Te inclusions in current CZT material could be critical in lowering the performance of thick (long-drift) CZT detectors, thereby limiting the size and efficiency of such detectors available to users [6-9]. The existence of Te inclusions and precipitates in CdTe and CdZnTe materials long has been known. In a comprehensive review, Rudolph [10] described Te inclusions as non-stoichiometric defects that formed during the melt growth of the crystals. They differ from Te precipitates that form during crystal cooling as a result of the nucleation of native defects. He noted that the sizes of Te precipitates measured by high-resolution transmission electron microscopy are 10-50 nm, while the typical diameters of Te inclusions are 1-2 μm, although sizes up to 100 um are observed in high-pressure and vertical-Bridgman grown CZT. The particles usually seen with IR microscopy (where the optical resolution is limited

Manuscript received January 3, 2008. This work was supported by U.S. Department of Energy, Office of Nonproliferation Research and Engineering, NA-22. The manuscript has been authored by Brookhaven Science Associates, LLC under Contract No. DE-AC02-98CH1-886 with the U.S. Department of Energy.

A. E. Bolotnikov, G. S. Camarda, A. M. Hossain, Y. Cui, and R. B. James are with Brookhaven National Laboratory, Upton, NY 11793 USA (phone: 631-344-8014; e-mail: bolotnik@bnl.gov).

N. M. Abdul-Jabbar is with University of Michigan, Ann Arbor, MI 48104 USA.

O. S. Babalola, E. M. Jackson, and H. C. Jackson are with Vanderbilt University, Nashville, TN 37235 USA.

J. A. James is with Tennessee Technological University, Cookeville, TN 38505 USA.

K. T. Kohman is with Kansas State University, Manhattan, KS 66506 USA.

A. L. Luryi is with Cornell University, Ithaca, NY 14853 USA.

to 1 μm) are attributed to Te inclusions. Their concentrations may exceed 10^7 cm^{-3}, but this still is several orders-of-magnitude less than that of the Te precipitates.

Previous discussions questioned whether or not Te inclusions affect the device's performance. Recently, we measured directly the charge trapped by individual inclusions [6,7] employing a highly collimated X-ray beam at the National Synchrotron Light Source (NSLS) at Brookhaven National Lab (BNL) [6,7]. Our findings provided clear evidence for the long-standing hypothesis of the cumulative negative effect of Te inclusions in thick CZT detectors. Modeling [8,9] electron transport in CZT material containing Te inclusions also confirmed that their successive addition can degrade energy resolution, and that the magnitude of the effect strongly depends on their size and concentration. Moreover, simulations predicted that inclusions of less than ~1-um diameter essentially behave as ordinary traps associated with point defects (native or impurities) in the material. Such defects trap the electrons but do not introduce fluctuations in the collected charge signals, so allowing for correction of the total charge loss using a depth-sensing technique. Interestingly, Te precipitates also may behave as point defects, and since their concentration in as-grown material can be high, they might control the *effective* mobility-lifetime product for both holes and electrons. Thus, to maximize the performance of CZT detectors, it is important to establish the limits of the sizes and concentrations of the inclusions as a function of the devices' thicknesses.

During our several CZT projects we have tested over 20 virtual Frisch-grid CZT detectors with thicknesses up to 20 mm. Theoretically, this type of device should provide an energy resolution of 0.7-1.5% FWHM at 662 keV depending on the device's thickness and the electron mobility-lifetime product [12-14]. However, the performance of some devices was significantly worse than expected. Visualization of these CZT samples via an IR microscope invariably revealed a high concentration of Te inclusions that, we believe, cause large fluctuations of the collected charge. These qualitative observations stimulated our further investigations, described in this article.

Here, we report on quantitative measurements of the correlation between the size and concentrations of Te inclusions and the devices' responses. We determined their sizes and concentrations with an automated IR microscopy system developed at BNL to screen semiconductor devices. The findings predict the extent to which Te inclusions can be tolerated in CZT crystals.

The samples used in these measurements were acquired from three vendors: eV Products, Redlen Technologies and Yinnel Tech, Inc., representing, respectively, three CZT growth techniques, viz., High-Pressure Bridgman (HPB), the Traveling Heater Method (THM), and Low-Pressure Bridgman (LPB). The high-quality crystals produced by these vendors afford the actual devices a spectral resolution close to the statistical limit.

Experimental

Detector testing

For these studies we used two batches of 22 parallelepiped-shaped CZT crystals with cross-sections of ~5x5 mm^2 and thicknesses of 10- and 12- mm, obtained from eV Products and Redlen for our other projects. We also acquired several specially selected high-quality crystals from Redlen and Yinnel Tech that had very low concentrations of Te inclusions. All the samples were specified as single crystals containing no twins, grain boundaries, or large (>50 um) inclusions; all were furnished with two planar contacts on the top and bottom sides.

Each crystal first was screened with our IR transmission microscopy system to obtain data on the sizes and concentrations of Te inclusions, and then configured as Frisch-ring detectors [11,12] for measurements with gamma rays. During these measurements, the detector was placed inside the standard eV Products device holder connected to a box containing the eV-5092 preamplifier that provided electronic noise of 3-4 keV FWHM (~0.5% at 662 keV). The shielding electrode was connected to the cathode and kept at zero potential, while the positive voltage was applied to the anode via a pogo-pin connector. Depending on the device's thickness, we applied 1000-2000 V biases to achieve the optimal performance from the device. The detectors were irradiated with gamma rays from a ^{137}Cs source located near the cathode. The data-acquisition system included a spectroscopy amplifier, MCA card, and standard NIM electronics.

According to our hypothesis, the width of the photopeaks in the pulse-height spectra should reflect the fluctuations of the collected charge due to electron trapping by Te inclusions within the material. The long drift distances of the electron clouds in these crystals should magnify this effect.

IR microscopy

The IR transmission microscopy system comprises a large field-of-view (FOV) microscope objective, a CCD camera, a motorized X-Y-Z translation stages, and a light source coupled with a wide-beam condenser for illuminating the samples (Fig.1). The CCD camera has a 7.8 x 10.6 mm^2 sensor area consisting of 2208x3000 pixels, each of 3.5x3.5 μm^2. The system can perform a one-, two-, or three-dimensional raster scan of a CZT crystal. At each XYZ position, an image of the area is taken and saved, and then the translation stages move the sample to the next position where this is repeated, and so on. The imaging setup allowed us to acquire stacks of images, each focused at a different depth of the crystal. At high magnifications, above x5, the depth of focus is comparable to the expected size of the inclusion (~10 m).

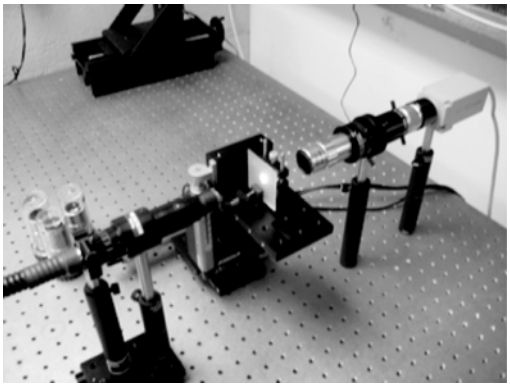

Fig. 1. A view (from the top) of the automated IR imaging system which includes a fiber-optic light source coupled with a wide-beam condenser illuminating the samples, a large field-of-view microscope objective, a CCD camera, and motorized translation stages.

The sizes and concentrations of Te inclusions were evaluated by taking images at five locations evenly distributed along the long side of the crystal from two perpendicular directions. We used a 5x magnification corresponding to a depth of focus (DOF) of 14 □m. After each scan in the Z direction, the system generated a stack of 45 images that cover a 1.1x1.5x5 mm^3 region extending from one surface of a crystal to the opposite side. The images were saved as monochrome high-resolution jpeg files, with 8-bit dynamic range.

An iterative algorithm was developed to identify inclusions and evaluate their sizes. CZT crystals are transparent to infrared light; however, using long wavelength light limits the feature's minimum size to ~1 μm. In the IR images, Te inclusions larger than 10 μm are seen as relatively sharp objects with triangular or diamond-like shapes depending on crystal's orientation and the illumination. In 3D images (pixel-intensity distributions), such inclusions are represented by 3-dimentional surfaces, in some cases comprised of two or more Gaussian-like functions. Small sized inclusions, below 5 μm, typically appear as blurred objects with surrounding artificial haloes that can be suppressed by passing an illuminating beam through a ground-glass diffuser. In a 3D image, small inclusions are represented by surfaces with a single Gaussian-like function. In this analysis, the geometrical size (diameter) of a Te inclusion is defined as the standard deviation of 2-D intensity distribution multiplied by a numerical factor of 2.356 (for true Gaussian distribution, this corresponds to the geometrical full width and half maximum).

The code was written in the Interactive Data Language (IDL) programming environment that is especially well suited for manipulating and processing images and has powerful input/output capabilities, along with variety of libraries for statistical analysis and plotting the results.

Since the actual size of the pixel in an x5-magnification image is 0.5x0.5 □m^2, which is ~2 times smaller than the resolving power of the optics used, four adjacent pixels were added together.

The first step in image processing was to subtract the slow variations of background and invert the original images so that the features representing inclusions were regions of high intensity (peaks). As an example, Fig. 2 depicts a 3D intensity distribution of the inverted image taken at x5 magnification. We used a Gaussian filter with a sigma of 1.5 pixel (□m) to suppress pixel noise, and a boxcar-averaging algorithm with a box size of 41x41 pixels (□m^2) to evaluate the background and its standard deviation.

We utilized the following algorithm for localizing the peaks. First, the routine identified the positions of all the local maxima in the image within circular neighborhoods with some given diameter, e.g., 20 pixels (□m), and an intensity exceeding 3 sigma of the background noise. To minimize computational time, this task was done by employing the image-manipulating routines only. Ref. [15] gives an example of applications of such routines (available in IDL) for small-feature analysis. Then, the system evaluates the image consisting of peak footprints measured at different intensity levels starting with the maximum. As the threshold level moves down step- by-step, more spots appear in the image and their areas continue to grow. Eventually, the footprint areas begin to overlap indicating that a local background level has been reached or, alternatively, that two peaks representing the same inclusion have finally merged. Using this process we could implement different logics for reconstructing the shapes of individual inclusions and correctly subtract the local variation of the background, e.g., an image of a small inclusion located in focus over a blurry out-of-focus image of a large inclusion. For small inclusions, <3 □m, represented by small narrow peaks, our decision on accepting or rejecting them was based on the local background noise and peak intensity, i.e., for acceptance, the peak intensity should exceed three standard deviations of the local noise.

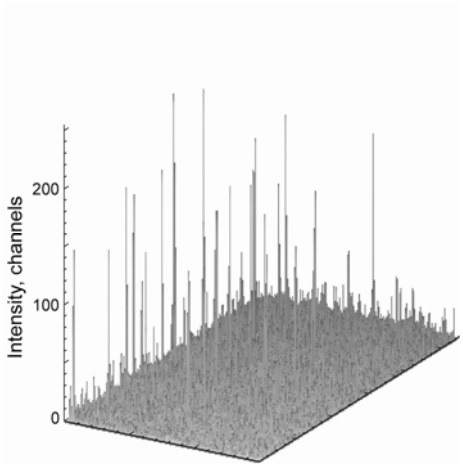

Fig. 2. Example of an intensity distribution of the 2208x3000 pixel IR image (inverted) of 1x1.5 mm^2 area of a CZT sample.

The output of the feature-determination routine is an array containing the following parameters: XY-coordinates of the found inclusion, its integrated brightness, and its diameter evaluated as full-width-at-half-maximum of peaks. Fig. 3 gives two examples of images with identified (circled) Te inclusions. Shown on the left are the original images, and on the right are the same images enhanced by applying the adaptive filter (available in IDL), which revealed faint out-of-focus features. As depicted, images may contain different kinds of features, noise, proper inclusions, and faint outlines of out-of-focus inclusions (large dark areas) that do not "belong" to the sample's current slice. The image at the bottom shows inclusions accumulated along the plane with high concentration of dislocations, which is an indication of a subgrain boundary.

The algorithm discards Te inclusions that are out-of-focus, counting only those in focus. This process entails two steps. First, a cutoff is applied on size/brightness to suppress the contribution of large objects of low brightness (Te inclusions out-of-focus). Second, the algorithm selects only one of the Te inclusions present at the same position in sequential layers.

For clarity, we use layer instead of image here. The same Te inclusion can appear in several neighboring layers (i.e., in both regions 1 and 2), but would be in focus only in one of them, or at least there would be a layer wherein that inclusion is in better focus than elsewhere. The algorithm selects the one in focus, and corrects for shifts of images. In this way, we are assured that each Te inclusion is counted only once. Also, to reduce contribution of faint inclusions caused by fluctuations in noise, we accepted the features seen in two or more images only.

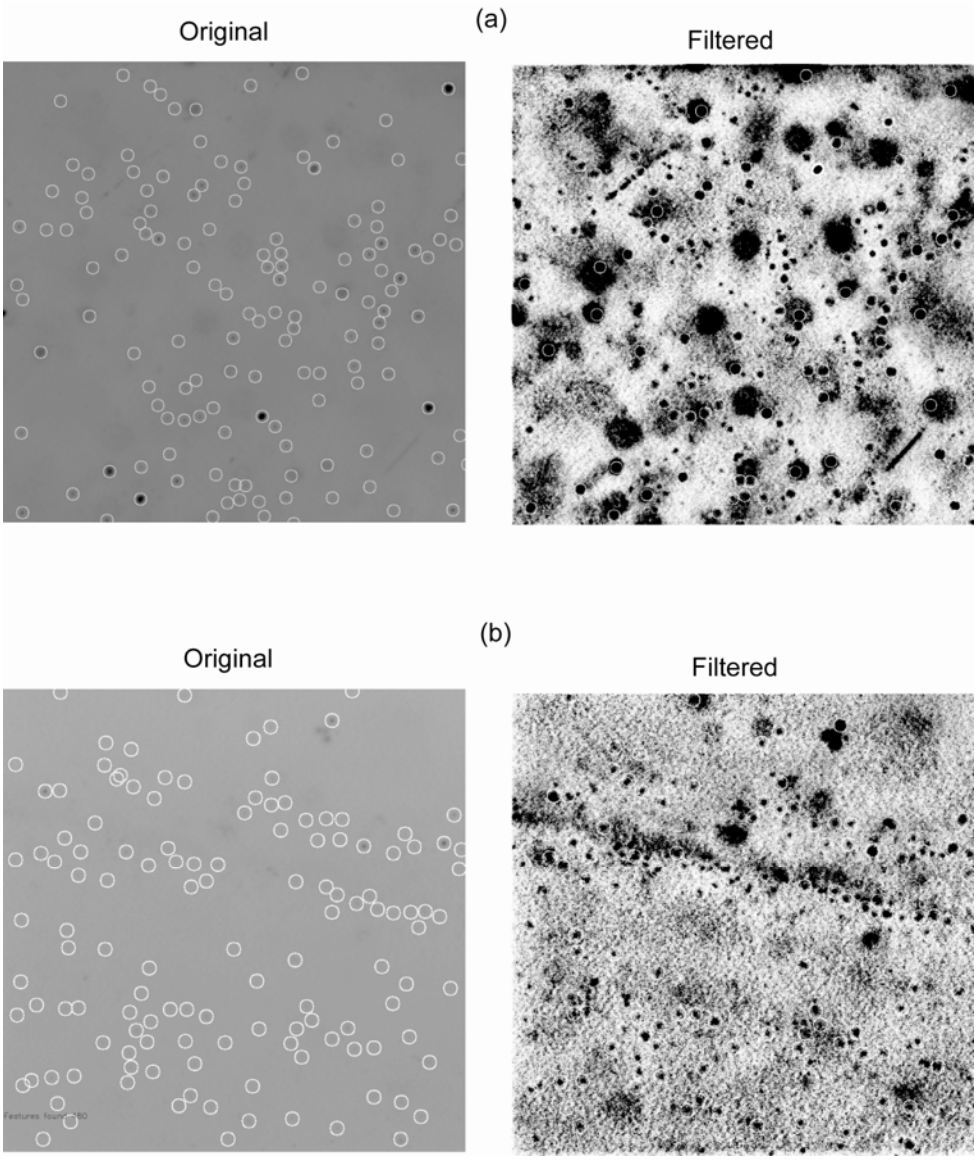

Fig. 3. Two examples of the IR images (a) and (b) with identified (circled) Te inclusions. The images cover 150x150 μm^2 CZT areas. The original images are shown on the left; the same ones, but with enhanced contrast, are shown on the right.

Then, by taking into account the FOV and the size of the z-scan step, the measured number of Te inclusions for each layer can be renormalized per cm^3. By varying the parameters of the algorithm, we estimated that the systematic errors introduced by the analysis routine were 15-30%.

We note that even though the optical system can locate and count inclusions with diameters as small as 0.5 μm, it cannot accurately determine their sizes if their diameter is <3 μm.

Results and Discussion

Distributions of the size and concentration of the Te inclusions

Here, we illustrate the ability of our IR microscopy system to measure the sizes and concentrations of Te inclusions in CZT samples. Fig. 4 shows one representative 3D distribution of Te inclusions evaluated for a 1x1.5x5 mm^3 section of a CZT sample. The inclusions decorating the linear dislocations (D) and the subgrain boundaries (S) can be clearly seen. Such defects generate local variations (on a millimeter-scale) in the inclusions' special distribution which otherwise would be randomly distributed within the sample.

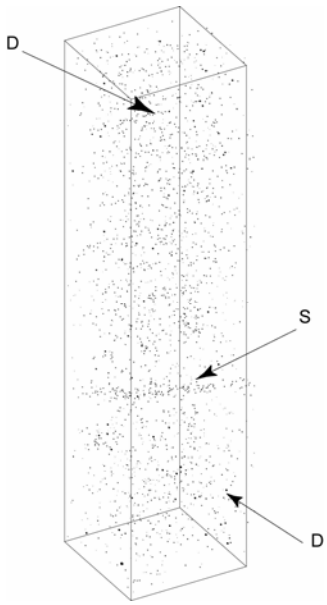

Fig. 4. 3D distribution of Te inclusions evaluated for a 1x1.5x5 mm^3 section of a CZT sample. Inclusions follow the dislocation patterns that result in local variations (on a sub-millimeter-scale) in their special distribution.

Another interesting feature in Fig. 4 is the continuous band filled with inclusions extending from one side of the crystal to the other; it is identified as a subgrain boundary (S). The presence of dislocations and subgrain boundaries in the sample was confirmed by white beam diffraction topography. We note that Te inclusions trapped by dislocations are normally seen as cellular structures in 2D images. They may affect the device's performance [2-4].

Fig. 5 plots the typical size distributions of Te inclusions evaluated for two representative samples from two CZT batches. Typically, the distributions both reach their maxima at the same diameter of ~5 μm, but the right edge of their distribution slopes differs, as is clearly seen on this semi-logarithmic scale. The total concentrations of inclusions were evaluated by integrating these distributions. Fig. 6 (a) shows the distributions of the concentration of inclusions in samples from two batches. (We reiterate that measurements were taken from each sample at five different locations over the crystal's length from two perpendicular directions.) In both batches, the values of concentrations lay within a narrow range between $1.5x10^5$ and $4x10^5$ cm^{-3}.

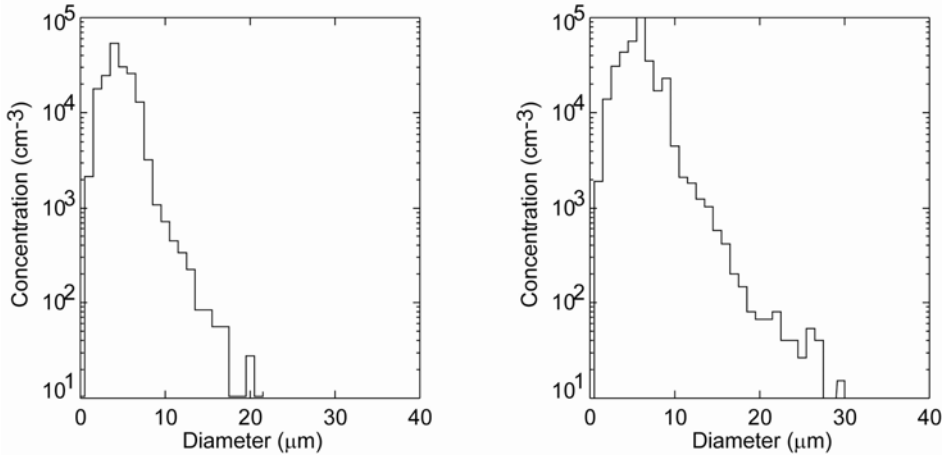

Fig. 5. Typical size distributions of Te inclusions evaluated for two representative samples from two CZT batches.

Variations of the concentration of Te inclusions within a sample also can impact a CZT device's performance, and thus, can be used to characterize the quality of the CZT material. Such variations are indicative of the presence of the extended defects in the crystals, e.g., dislocations encompassing inclusions. Fig. 6(b) shows typical density variations in Te inclusions, evaluated by counting the total numbers (all sizes) of inclusions inside 125 1x1x1 mm^3 cubes comprising the 25 1x1x5 mm^3 sections screened for each of the crystals. A difference is clearly apparent between the distributions for CZT samples taken from the two batches. For comparison, Fig. 6(c) shows a theoretical distribution calculated assuming a random distribution of inclusions.

Correlation between the size and concentration of Te inclusions and energy resolution

Based on the results obtained from our measurements with the highly collimated X-ray beam, we proposed a theoretical model [9] considering Te inclusions as non-transparent to the electron clouds and having no effect on the electric distribution inside a detector. The model very accurately reproduced the experimental results obtained from the x-ray scans of thin, <2 mm, planar detectors, and predicted a strong cumulative effect of randomly distributed inclusions on the performance of the thick (long-drift) detectors like Frisch-ring or pixel devices.

As mentioned in the introduction, two effects are associated with the Te inclusions. Firstly, the inclusions reduce the total amount of the collected charge as the electron cloud drifts towards the anode in a similar manner as do the traps associated with point defects. The total amount of the lost charge is proportional to the drift distance traveled by the electron cloud, and can be described by an exponential decay function with a charge attenuation length, □. Secondly, because the inclusions trap many electrons per interaction with electron clouds, they cause large fluctuations in the collected charge. Using our model that treats Te inclusions as non-transparent spheres, we calculated the charge attenuation length, □, and the expected broadening of the photopeak in % of FWHM at 662 keV, caused by inclusions in a 15-mm thick detector, versus the inclusions' diameters and concentrations. The curves in Fig. 7 represent the theoretical dependences calculated for 1-, 3-, 5-, 10-, 15-, and 20-μm *effective* diameters of inclusions that were assumed to be the same (a) and one half (b) of their actual diameters measured with IR microscopy. (A reason for showing the two effective diameters will be discussed in the next section). The electric field's strength inside the device was assumed to be 2000 V/cm. We also added an intrinsic noise of 0.5% at 662 keV associated with electron-hole pair production statistics. When calculating the fluctuations in the collected charge, the charge losses due to trapping were corrected proportionally to the electron cloud's drift distances so the positions of the photopeak evaluated for different interaction depths were always at the same position. Because of our assumption about the effective diameters of Te inclusions used in the model, the curves in Fig. 7 should be considered as lower and upper limits.

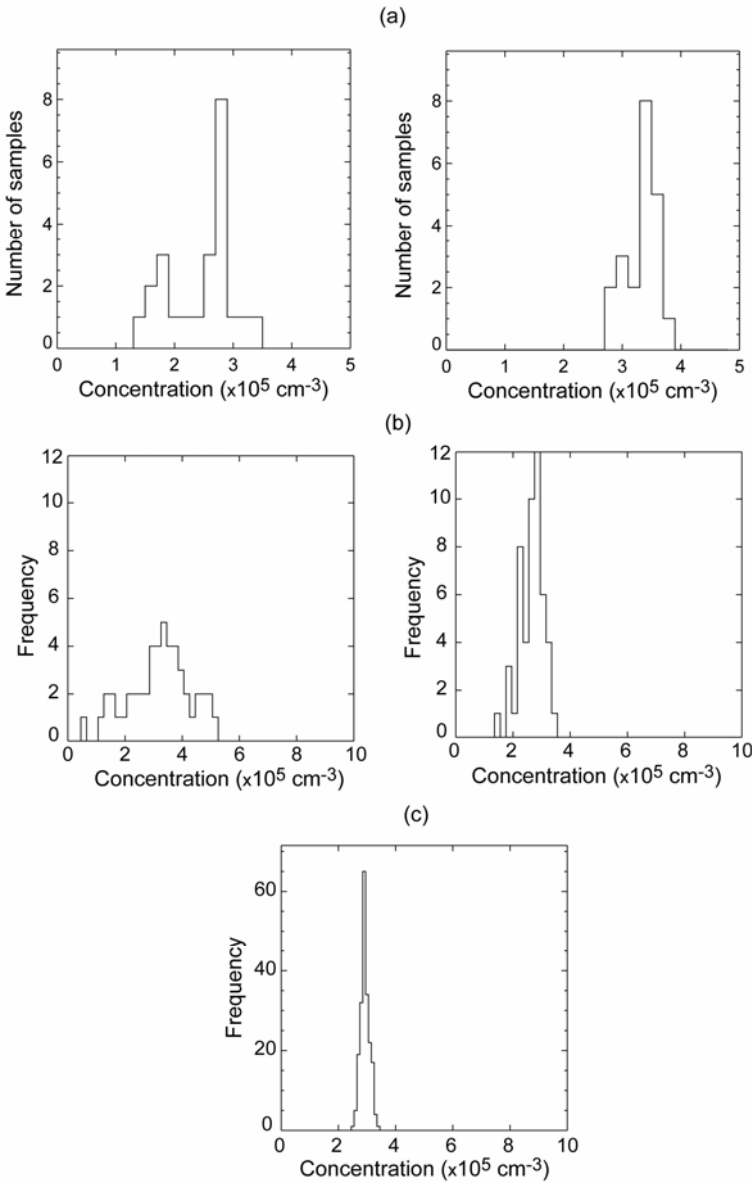

Fig. 6. (a) Distributions of the concentrations evaluated for the samples from two batches. (b) Variations of the concentrations of inclusions within individual samples from the two batches. (c) Theoretical distribution expected for random distribution of Te inclusions.

Results from pre-selected high-quality samples

The results obtained from testing pre-selected high-quality Redlen and Yinnel Tech detectors were used as a baseline for the further analysis. These carefully chosen crystals were free from subgrains, had an electron $\mu\tau$-product of >3x10^{-2} cm^2/V, and their IR images show no cellular patterns of Te inclusions, indicating the absence of large dislocations. In other words, we assumed that Te inclusions were the only prominent macroscopic defects in these samples. Specifically, the two samples of 4x4x11 mm^3 and 5x5x14 mm^3 that exhibited superior spectral responses only contained small inclusions of less than 3 μm with concentrations of 1.2x10^6 cm^{-3} and 2.7x10^6 cm^{-3}, correspondingly. The noise-subtracted energy resolutions measured for these detectors were, respectively, 0.7 and 1.1% FWHM at 662 keV, entirely attributable to charge variations due to continued electron trapping by point defects and device geometry. Both the measurements and the calculations demonstrate that Te inclusions with diameters of $\leq$3 μm and concentrations of $\leq$3x10^6 cm^{-3} have no effect on the energy resolution of CZT

detectors with thicknesses up to 14 mm (data not shown).

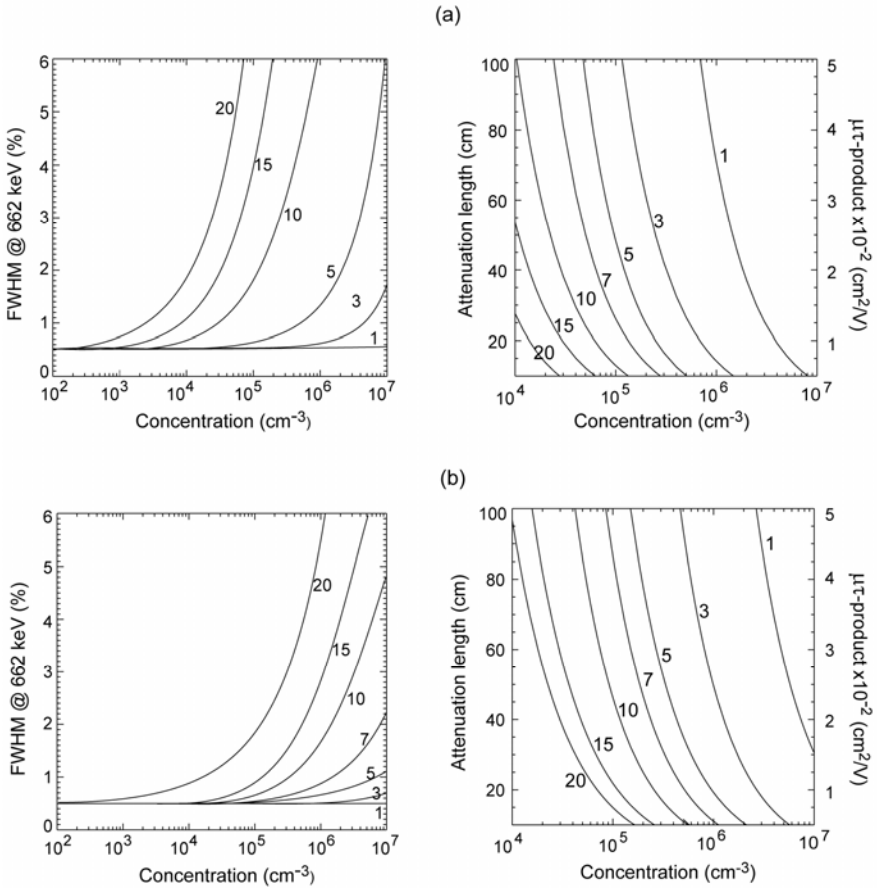

Fig. 7. The effect of broadening of photopeak, FWHM (%) at 662 keV (left) and charge attenuation length (right), resulted from the fluctuation of charge loss due to Te inclusions versus their concentration calculated for 1-, 3-, 5-, 7-, 10-, 15-, and 20-μm inclusions for the two cases of the effective diameters of inclusions: (a) equal to, and (b) 1/2 of their actual diameters. The detector's thickness is 15 mm, and electric-field strength is 2000 V/cm. The variation of the charge losses due to different locations of interaction points was subtracted from FWHM (bi-parametric correction).

Results from two batches of the standard commercial crystals

As discussed above, Te inclusions with diameters <3 μm have no effect on charge transport at least up to a concentration of $3x10^6$ cm^{-3}. On the other hand, the effectiveness of the algorithm in identifying small inclusions is not as good as it is for the larger ones. Thus, in a further analysis we set a 3-μm threshold to discard small-size inclusions and minimize potential errors.

For the analysis we excluded crystals with poor spectral responses for which energy resolution was greater than 3%. These crystals contained twins, subgrain boundaries, or large areas of dislocations, which we identified with white beam diffraction topography and IR microscopy. We included the detectors that showed good spectral responses with narrow, symmetrical photopeaks.

Fig. 8(a) illustrates the correlation between noise-subtracted energy resolution and concentration of Te inclusions evaluated for samples from two CZT batches. The data points form two separate groups corresponding to different crystal thicknesses. For each of the groups, no correlations were apparent. Fig. 8(b) shows the same data plotted versus the total area of Te inclusions per cm^3. The total area takes into account both the sizes and the concentrations of inclusions. As in the previous case no correlations were apparent. On average, for 10- and 12-mm thick crystals the noise-subtracted energy resolutions were, respectively, 1.1 and 1.4% (FWHM at 662 keV) measured at 1000- and 1500-V. Again, as with the pre-selected detectors, these values can be entirely attributed to the dependence of output

signals on the locations of the interaction points. This dependence results from the interplay between the inefficiency of shielding of the virtual Frisch-grid and charge loss due to electron trapping that compensate each other. The simulations [13] predict that this dependence alone can give a geometrical FWHM of the device's response function ranging between 0.5 to several percent, depending on the $\mu\tau$-product and detector's thickness. By fitting the dependences of output signals versus drift time (correlation curves) we found that the crystals from both batches had a 20-30 μs electron lifetime, equivalent to 3.0-5.0 % of the total amount of change loss across a device; this corresponds to 0.9-1.3% (FWHM at 662 keV) for 10-mm detectors, and 1.0-1.6 % for 12-mm ones. We note that the charge loss due to both the point defects and inclusions can be corrected to preserve good energy resolution by using the depth-sensing techniques.

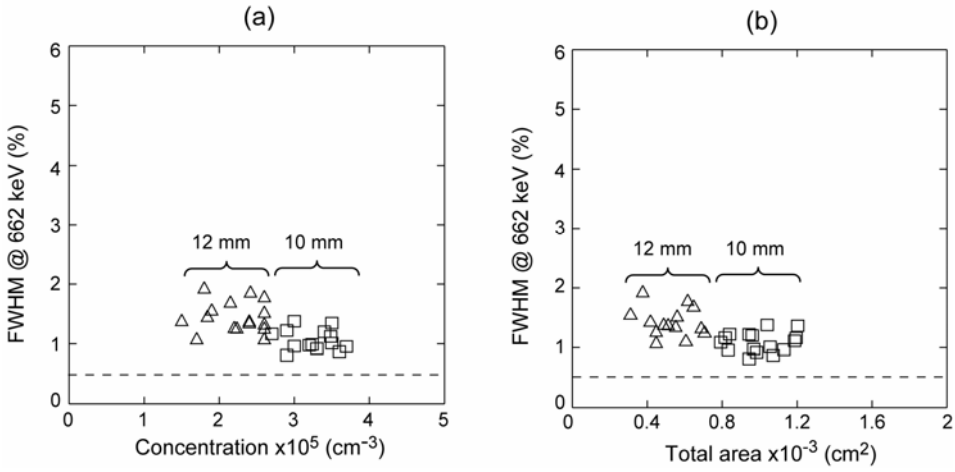

Fig. 8. Noise-subtracted energy resolution versus (a) concentration of Te inclusions and (b) total area of inclusions per cm^3 evaluated for the samples from two CZT batches. The statistical limit, ~0.5%, is indicated by a dashed line

Another factor contributing to the FWHM is the density variations of Te inclusions. As illustrated in Fig. 6(b) the crystals from one batch (12-mm long detectors) have a broader distribution of the concentration of inclusions. Furthermore, other extended defects such as dislocations also may contribute (not discussed here). In other words, the small variations of the integrated concentrations of Te inclusions can be overshadowed by other factors. Perhaps a more accurate analysis based on systematic measurements of the size and spatial variations of Te inclusions can reveal the correlations.

To adjust our model, we calculated the linear attenuation and fluctuations of the collected charge for several samples and compared them with the measured $\mu\tau$-products (or life times) and peak widths. In these calculations we took the measured size distribution of Te inclusions (Fig. 5) as the inputs for the model. The simulated charge fluctuations were negligible, well below 0.5%. In contrast, the simulations predicted a strong attenuation of the electrons that would alone, without additional electron trapping by the point defects, account for the observed charge loss in the samples. This implies that the effective size of Te inclusions used in the model should be less than their actual sizes seen with IR microscopy.

The continuous charge loss in CZT material containing Te inclusions can be described by

$$Q = Q_0 \exp\left\{-l\left(\frac{1}{\mu\tau E}+\frac{1}{\lambda}\right)\right\}, \qquad (1)$$

where l is the drift distance of the electron cloud, E is the electric field strength, and λ is the attenuation length that describes (at least in the first approximation) charge loss due to inclusions (see discussion above). Using Eq. (1) we can modify the Hecht relationship [16] by replacing τ with $\tau/(1+\mu\tau E/l)$ and then evaluate the electron's lifetime τ and attenuation length λ. However, because of a strong correlation between τ and λ the fitting routine cannot be applied directly. Indeed, the Hecht equation normally is used to fit data measured with thin CZT crystals, wherein the charge loss caused by extended defects is completely hidden from the analysis.

To overcome this problem, we proposed employing the modified Hecht equations to fit data measured for two detectors made from the same crystal: a thin one, ~2 mm; and a thick one, ~10 mm. The former would be used to calibrate the electronics (i.e., find the total produced charge Q_0), and evaluate the $\mu\tau$. As these parameters become known, the thick crystals can be used to evaluate λ.

Unfortunately, we could not follow this procedure strictly; we used thin and thick detectors but fabricated from different crystals. The thin detector was employed to calibrate the electronics only while the parameters $\mu\tau$ and λ were found from the second fitting. We applied this procedure to fit data measured for 5 representative detectors from the 10-mm CZT batch. Since the Hecht equation is applied to the planar detectors, we removed the shielding electrodes from these detectors and placed a ~2-cm diameter metal disc on top of their anodes during the measurements. The detectors were illuminated with 59.5-keV photons; the shaping time of the amplifier was 10 μs. On average, the fittings (an example is shown in Fig. 9) gave ~20 μs for the electron lifetime and ~100 cm for the

electron attenuation length. Due to the drawback of the fitting procedure, the value for the charge attenuation length should be treated as a first-order estimate.

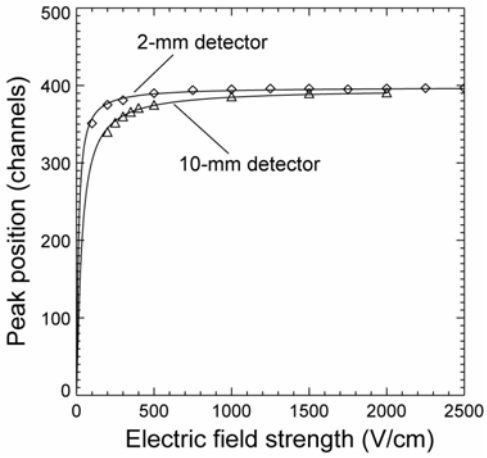

Fig. 9. Application of the modified Hecht equation to fit the data from 2- and 10-mm thick CZT detectors. The detectors were illuminated with 59.5-keV photons; the shaping time of the amplifier was 10 μs.

Next, we adjusted the effective diameters of Te inclusions so the model would reproduce the attenuation lengths measured for the 10-mm thick detectors. We found that the effective diameter should be ~2 times smaller than the actual one. With this adjustment, we recalculated the expected dependencies of the attenuation length and the expected broadening of the photopeak in % of FWHM at 662 keV, caused by Te inclusions in a 15-mm thick detector, versus their diameters and concentrations shown in Fig. 7(b). All together, the plots in Fig. 7 give the lower and upper estimates of the effects of the randomly distributed Te inclusions expected in thick CZT detectors.

Conclusions

Based on the statistics from ~50 samples of high-quality commercial CZT crystals intended to be used as nuclear radiation detectors, we evaluated the size distributions and concentrations of Te inclusions and correlated these data with spectral responses of actual devices.

No correlations were identified between the sizes and concentrations of Te inclusions and the width of the peaks measured with these particular samples. The measured values of the FWHM could be entirely attributed to the electron trapping by point defects and the device's geometry. Our results gave the lower limits on the acceptable levels of Te inclusions in CZT detectors.

The charge trapping by Te inclusions is described by the exponential function of the electron cloud's drift distance with a charge attenuation length—the free parameter that can be evaluated by employing the modified Hecht relation.

By comparing the measured and modeled attenuation lengths, we adjusted the free parameter in our model and calculated the effects of Te inclusions on energy resolution expected in thick devices of ~15 mm.

We found that Te inclusions with diameters of less than 3 μm can be virtually neglected. Their presence in the material at concentrations lower than 10^6 does not affect significantly the detector's performance, e.g., a FWHM of less than 1% was obtained for 662 keV for a 11-mm long Frisch-ring detector. At higher concentrations or in thicker devices, the cumulative effect of small inclusions can be corrected by using a depth-sensing technique.

These results provide insight into the critical role of the Te inclusions, whose presence in current CZT material is related to their growth under non-stoichiometric conditions. Hence, these data are very important to the CZT crystal growers because once these defects are understood and can be controlled, large-volume, several cm^3, CZT detectors will become available to users.

ACKNOWLEDGMENT

We would like to thank Drs. C. Szeles and R. Smith from eV Products, Dr. H. Chen from Redlen Technologies, and Dr. L. Li from Yinnel Tech for the fruitful discussions.

REFERENCES

[1] R. B. James, T. E. Schlesinger, J. C. Lund and M. Schieber, "Cadmium Zinc Telluride Spectrometers for Gamma and X-Ray Applications", in Semiconductors for Room Temperature Nuclear Detector Applications, Vol. 43, edited by R. B. James and T. E. Schlesinger (Academic Press, New York, 1995), p. 334.

[2] C. Szeles and E. E. Eissler, "Current issues of High-pressure Bridgman growth of semi-insulating CdZnTe", in Semiconductors for Room Temperature Radiation Detector Applications II, Vol. 487, edited by R. B. James, T. E.

Schlesinger, P. Siffert, W. Dusi, M. R. Squillante, M. O'Connell and M. Cuzin (Materials Research Society, Pittsburgh, PA, 1998), pp. 3-12.

[3] J. R. Heffelfinger, D. L. Medlin, and R. B. James, "Analysis of Grain Boundaries, Twin Boundaries and Te Inclusions in Cadmium Zinc Telluride Grown by High-Pressure Bridgman Method", in Semiconductors for Room Temperature Radiation Detector Applications II, Vol. 487, edited by R. B. James, T. E. Schlesinger, P. Siffert, W. Dusi, M. R. Squillante, M. O'Connell and M. Cuzin (Materials Research Society, Pittsburgh, PA, 1998), p. 33.

[4] C. Szeles, S. E. Cameron, J.-O. Ndap, W. C. Chalmers, "Advances in the crystal growth of semi-insulating CdZnTe for radiation detector applications", *IEEE Trans. Nucl. Sci.,* NS 49, n.5, pp. 2535-2540, 2002.

[5] M. Amman, J. S. Lee, and P. N. Luke, "Electron trapping nonuniformity in high-pressure-Bridgman-grown CdZnTe", *J. Appl. Phys.,* vol. 92, pp. 3198-3206, 2002.

[6] G. A. Carini, A. E. Bolotnikov, G. S. Camarda, G. W. Wright, L. Li, and R. B. James, "Effect of Te inclusions on the performance of CdZnTe detectors", Appl. Phys. Lett. 88, p. 143515, 2006.

[7] G. S. Camarda, A. E. Bolotnikov, G. A. Carini, and R. B. James, "Effects of Tellurium Inclusions on charge collection in CZT Nuclear Radiation Detectors", in Countering Nuclear and Radiological Terrorism, edited by S. Aprkyan and D. Diamond, Springer, 2006, pp. 199-207.

[8] A. E. Bolotnikov, G. S. Camarda, G. A. Carini, Y. Cui, L. Li, and R. B. James, "Modeling the geometrical effects of Te precipitates on electron transport in CdZnTe", Nucl. Instr. Meth. A 571, pp. 687–698, 2007.

[9] A. E. Bolotnikov, G. S. Camarda, G. A. Carini, Y. Cui, K. T. Kohman, L. Li, M. B. Salomon, and R. B. James, "Performance-limiting Defects in CdZnTe Detectors", *IEEE Trans. Nucl. Sci.,* NS 54, n 4, pp. 821 – 827, 2007.

[10] P. Rudolph, Non-stoichiometry related defects at the melt growth of semiconductor compound crystals – a review", Cryst. Res. Technol. Vol. 38, n. 7-8, pp. 542-554, 2003.

[11] W. J. McNeil, D. S. McGregor, A. E. Bolotnikov, G. W. Wright and R. B. James, "Single-Charge-Carrier-Type Sensing with an Insulating Frisch Ring CdZnTe Semiconductor Radiation Detector", Appl. Phys. Lett. 84, pp. 1988-1990, 2004.

[12] A. E. Bolotnikov, G. C. Camarda, G. A. Carini, M. Fiederle, L. Li, D. S. McGregor, W. McNeil, G. W. Wright, and R. B. James, "Performance Characteristics of Frisch-Grid CdZnTe Detectors", *IEEE Transactions on Nuclear Science*, NS 53, n.2, pp. 607-614, 2006.

[13] A. E. Bolotnikov, N. M. Abdul-Jabbar, S. Babalola, G. S. Camarda, Y. Cui, A. Hossain, E. Jackson, H. Jackson, J. R. James, A. L. Luryi, and R. B. James, "Optimization of virtual Frisch-grid CdZnTe detector designs for imaging and spectroscopy of gamma rays", Invited Paper, in Proceedings of SPIE Hard X-Ray and Gamma-Ray Detector Physics IX, Vol. 6702, edited by R. B. James, A. Burger, L. A. Franks, (SPIE, San Diego, CA, 2007), pp. 670603-1 – 670603-14.

[14] A. E. Bolotnikov, G. S. Camarda, G. A. Carini, M. Fiederle, L. Li, G. W. Wright, and R. B. James, "Performance Studies of CdZnTe Detector by Using a Pulse-Shape Analysis", Invited Paper, in Proceedings of SPIE Hard X-Ray and Gamma-Ray Detector Physics VII, edited by R. B. James, L. A. Franks, and A. Burger (SPIE, San Diego, CA, 2005), 59200K-1 – 59200K-12.

[15] J. C. Crocker and D. G. Grier, "Methods of digital video microscopy for colloidal studies", J. Colloid Interface Sci., Vol. 179, pp. 298-310, 1996.

[16] K. Hecht, "Zum Mechanismus des lichtelektrischen Primärstromes in isolierenden Kristallen," Z. Phys. **77**, pp. 235–245, 1932. See also G. Knoll, Radiation Detection and Measurement, p. 480, 3rd ed, Wiley, New York (2000).